Precision Engineering 83 (2023) 112–123

Contents lists available at ScienceDirect

Precision Engineering

journal homepage: www.elsevier.com/locate/precision

A piezoelectric load-sharing-based platform for measuring dynamic six-dimensional forces/moments of large equipment in spacecraft

Chengbo Zhou [a,b], Mingyi Xia [a,*], Zhenbang Xu [a,b,**]

[a] Changchun Institute of Optics, Fine Mechanics and Physics, Chinese Academy of Science, Jilin Changchun, 130033, China
[b] Center of Materials Science and Optoelectronics Engineering, University of Chinese Academy of Sciences, Beijing, 100049, China

ARTICLE INFO

Handling Editor: Prof. R. Leach

Keywords:
Vibration
Force measurement platform
Load sharing
Heavy load
Self decoupling

ABSTRACT

Measuring dynamic force is essential for improving equipment accuracy in the aerospace industry. This work presents a self-decoupled, load-sharing-based measurement platform for measuring dynamic force from large sources. Utilizing a load-sharing column increases the rigidity and load capacity of the platform. The measurement principle is thoroughly described. Moreover, the effects of the structural parameters of the platform on performance are then analyzed using finite element analysis, while the feasibility of the measurement principle is verified and an optimal set of structural parameters is obtained using response surface methodology. Finally, the load-sharing-based measuring platform is manufactured based on the analysis. According to the experimental findings, the proposed platform with the column has a 59.7% higher load capacity and a measured fundamental frequency of 1696 Hz. The measuring platform also exhibits strong static and dynamic linearity, high self-decoupling, and an average dynamic measurement error of less than 6%.

1. Introduction

When compared to other traditional cameras, the Chinese Space Station Telescope's (CSST) performance represents a substantial advancement [1–4]. A case in point is that CSST plans to cover around 17,500 square degrees of sky with a resolution of 0.15" [5] while exploring important cosmological problems, such as dark matter and dark energy [6]. Moreover, CSST has high measurement precision and a field of vision that is about 5–8 times wider than that of Hubble [7]. Hence, micro-vibration may significantly affect CSST's excellent performance [8,9]. As a result, it is important to measure and assess the micro-vibration dynamic disturbance forces on the ground. Additionally, each functional module has a diameter of more than 1 m, and the weight and size of the moving elements on spacecraft have increased [10,11]. Given the foregoing, a measurement platform with a bigger mounting area, greater load capacity, higher fundamental frequency, and acceptable measurement accuracy is required.

There are some studies that can be used as references for the above requirements. The classic strain-gauge-based force measurement systems [12–16] in the past have good static characteristics, stability, a large measurement range, and high accuracy. Take Huang [17] as an example, he developed a three-dimensional strain-gauge-based force measurement platform with mutually perpendicular and independent elastic elements to measure high-frequency grinding forces. This platform has the advantages of a high fundamental frequency and low coupling, but it only works on the premise of the small platform size (60 × 60 × 7 mm^3). Apart from that, it is challenging to obtain high load capacity and sensitivity for strain-gauge-based devices because doing so results in noise interference being introduced into the measuring signal (the sensitivity of the elastomer is decreased), necessitating a compromise between the two [1]. Contrarily, piezoelectric ceramics offer good dynamic mechanical properties during tests of heavy loads and increase the platform's load capacity while maintaining high sensitivity. Therefore, piezoelectric components are used in the majority of contemporary heavy-load force measurement platforms. The Stewart platform [18] has been widely employed in previous investigations of piezoelectric measuring devices. Yet due to the platform's low structural rigidity, extreme instability, difficulty of installation, high processing costs, and other drawbacks [2,10], its application is limited. More orthogonal parallel distributions are used by other measuring equipment [19–25]. Among others, Li [19] presented a piezoelectric six-dimensional heavy-load force/moment sensor that has a high fundamental

* Corresponding author.
** Corresponding author. Changchun Institute of Optics, Fine Mechanics and Physics, Chinese Academy of Science, Jilin Changchun, 130033, China.
E-mail addresses: xiamingyi@ciomp.ac.cn (M. Xia), xuzhenbang@ciomp.ac.cn (Z. Xu).

https://doi.org/10.1016/j.precisioneng.2023.05.009
Received 9 March 2023; Received in revised form 8 May 2023; Accepted 30 May 2023
Available online 30 May 2023

frequency and low coupling. However, the fundamental frequency of the device will dramatically decrease as the mounting area and load's weight rise, making it difficult to achieve the measurement requirements with a straightforward four-point support. For this purpose, Li [20,21] investigated two different kinds of force/moment sensors with load-sharing rings, both of which displayed good performance in terms of accuracy and load capacity. Whereas, the equivalent stiffness of dozens of components is introduced in the derivation of the load sharing ratios in the article [20], making the calculation prone to large errors with reality to the extent that the mathematical model can not be used directly for measurement. Furthermore, the mathematical model cannot be applied intuitively as a design guide because it is tough to determine how structural characteristics affect the impact of load sharing. Sector-shaped piezoelectric ceramics are delicately employed for decoupling in the article [21], but customizing non-regular piezoelectric ceramics is complicated and expensive. Moreover, Li's two force/moment sensors are better suited for installation at the end of a robotic arm and can not accommodate large and heavy vibration sources. For the eight-point parallel-support sensor of Liu [22], a theoretical model was developed, but due to the over-redundant support, it is difficult to guarantee that the manufactured sensor closely matches the mathematical model. Thus, calibration experiments are required to correct the mathematical model for better measurement accuracy in applications. These researchers do not take into account the influence of the dynamic characteristics of the sensors themselves on the measurement, and their design approach cannot be used as a reference for the design of dynamic measurement equipment. A platform for measuring dynamic disturbance forces from large mass and volume vibration sources has recently been proposed by Xia [10]. The lower limits of the measured forces/moments are 4.1×10^{-4} N and 4.5×10^{-5} Nm, respectively, and the upper limit of the load capacity is 40 kN. However, its measuring principle leads to redundant measurements and systematic errors. To sum up, there are various structural designs and measurement principles for different measuring device applications, but it is tough for the current devices to satisfy the required measurement needs.

This research presents a novel piezoelectric load-sharing-based measurement platform that has been improved over earlier theories. First, a load-sharing column is set up to resolve the contradiction that the large mounting surface and high fundamental frequency are a pair of opposing indicators. Besides, systematic work has been done on the measurement principle and the analysis of the structural parameters. The platform's fundamental design is described in Section 2. Section 3 details the measurement principle and measurement coefficients of the platform. Section 4 describes the influence of structural parameters on the working performance of the platform and optimizes the structural parameters of the platform using response surface methodology. The tests carried out to assess the platform's performance are shown in Section 5. Section 6 includes conclusions.

2. Design of the measuring platform

The fundamental structure of the load-sharing-based measuring platform, shown in Fig. 1, consists of a load platform (mounting surface: 400×400 mm^2), a load-sharing column, four sensors, and five installation bases. The load-sharing column is mounted parallel to the sensors and placed in the middle of the lower surface of the load platform, with the four sensors spread evenly around it. In order to circumvent the flatness requirements of vast areas and cut processing costs, five tiny bumps are set on the load platform's lower surface, which connect the sensors and the load-sharing column. Electron beam welding is used to join the sensors and load-sharing column between the installation bases and the load platform. The installation bases are fixed to the vibration isolation platform, and the vibration sources can be mounted to the load platform for dynamic disturbance force measurements.

The sensors are made up of force sensing elements, rigid insulation layers, and an installation shell, as seen in Fig. 2(a). Sensor A uses force sensing elements with compression or shear effects, while sensor B solely utilizes force sensing elements with compression effects. Both sensors are sealed with resin by the preload mechanism. This indicates that sensor A can measure forces in the X, Y, and Z directions, whereas sensor B can only detect forces in the Z direction. Fig. 2(b) depicts the arrangement of sensors A and B within the measurement platform, with sensors 1 and 2 belonging to sensor A and sensors 3 and 4 to sensor B. The shear effect crystals are costly, so only two sensors A are set up in order to reduce the cost and completely measure the six-dimensional forces in space.

As for the three-sensor-supported measurement platform, it will drastically lower its fundamental frequency while keeping the size of the mounting surface, leading to severe coupling between the vibration source and the platform, and lowering measurement accuracy. A three-sensor-supported platform's mathematical model is also less transparent and easy to comprehend than a four-sensor-supported platform's. Furthermore, if the four sensors are non-uniformly distributed, it is difficult, on the one hand, to optimize the structure; on the other hand, the non-uniformly distributed platform is not as stiff as a uniformly distributed platform; and, above all, it is difficult to carry out the derivation of subsequent theoretical models.

3. Measurement principle

When six-dimensional forces/moments are applied to the load platform and then transferred to the load-sharing column and sensors, the assumptions are as follows.

(1) The load platform and installation bases are considered rigid bodies;
(2) The load-sharing column and sensors are treated as elastomers;
(3) The influence of machining and mounting errors on the lever balance principle is not considered;
(4) The effect of the wire hole in the side of the sensor is disregarded.

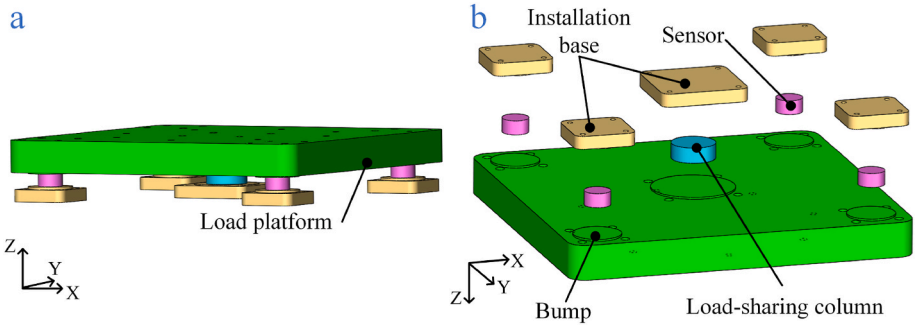

Fig. 1. Basic structure of the load-sharing-based measuring platform: (a) front view; (b) exploded bottom view.

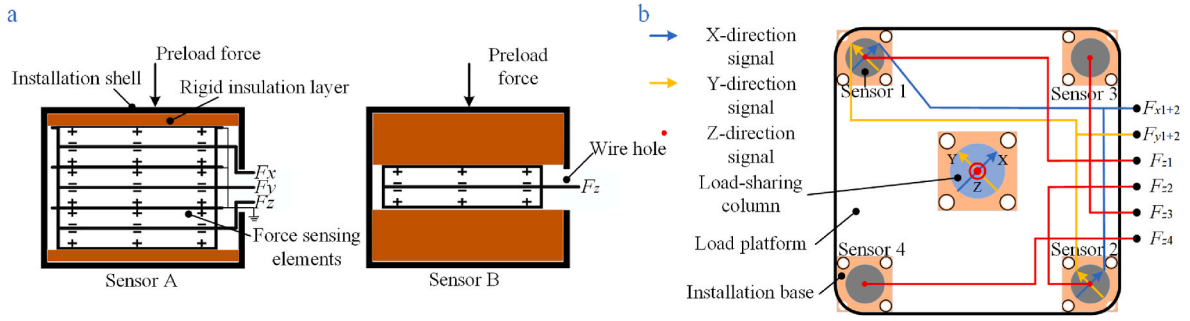

Fig. 2. Principles of the platform: (a) structure of sensors A and B; (b) distribution and outputs of sensors.

According to Fig. 2(b), the forces/moments acting on the sensors can be obtained based on the following assumptions and static equilibrium conditions:

$$\begin{cases} Fx - m = 2Fx1 + 2 \\ Fy - m = 2Fy1 + 2 \\ Fz - m = Fz1 + Fz2 + Fz3 + Fz4 \\ Mx - m = Ra(Fz1 - Fz2) \\ My - m = Ra(Fz4 - Fz3) \\ Mz - m = 2Ra(Fx2 - Fx1) \end{cases} \tag{1}$$

where the subscript m denotes measured, F_{x1+2} denotes the sum of the output forces from sensors 1 and 2 in the X direction, and F_{y1+2} denotes the sum of the output forces from sensors 1 and 2 in the Y direction. The relationship between sensor output voltages and forces can be obtained through calibration experiments.

Because of the existence of the load-sharing column, the forces/moments measured by the sensors are not equal to the forces/moments acting on the load platform. There is a relationship between the two:

$$\begin{cases} Fx - m = \mu FxFx \\ Fy - m = \mu FyFy \\ Fz - m = \mu FzFz \\ Mx - m = \mu MxMx \\ My - m = \mu MyMy \\ Mz - m = \mu FzMz \end{cases} \tag{2}$$

where F_x, F_y, F_z, M_x, M_y and M_z are the forces and moments acting on the load platform, and μ is the measurement coefficient. If μ can be obtained, the forces/moments on the load platform can be calculated by Equations (1) and (2).

The measurement coefficients are obtained through the law of conservation of energy, as shown in Equation (3):

$$\sum_{i=1}^{n} \frac{1}{2} Fi\Delta i = \sum \int \frac{F^2(x)\mathrm{d}x}{2EA} + \sum \int \frac{T^2(x)\mathrm{d}x}{2GI} + \sum \int \frac{M^2(x)\mathrm{d}x}{2EI} + \sum \int \frac{\eta V^2(x)\mathrm{d}x}{2GA} \tag{3}$$

where the left term of the equation represents the work done by the generalized forces acting on the load platform and the right terms represent the sum of the axial strain energy, the sum of the bending strain energy, the sum of the torsional strain energy, and the sum of the shear strain energy on the elastomers, respectively. Equation (3) shows that the work done by generalized forces is equal to the energy stored in the elastomers without thermal effects.

Since the measurement platform is symmetrical, the calculations of F_x and F_y, M_x and M_y are similar, only the derivations of μ_{Fx}, μ_{Fz}, μ_{My} and μ_{Mz} need to be performed.

3.1. Measurement coefficient of F_z

Fig. 3(a) shows the deformation of the platform when subjected to F_z. The load-sharing column and the sensors are subjected to the forces in the same way, which gives:

$$Fz = 4Fzp + Fzl \tag{4}$$

where F_{zl} is the axial force acting on the load-sharing column and F_{zp} is the axial force acting on the piezoelectric sensor.

According to the energy method, Equation (5) can be obtained as follows:

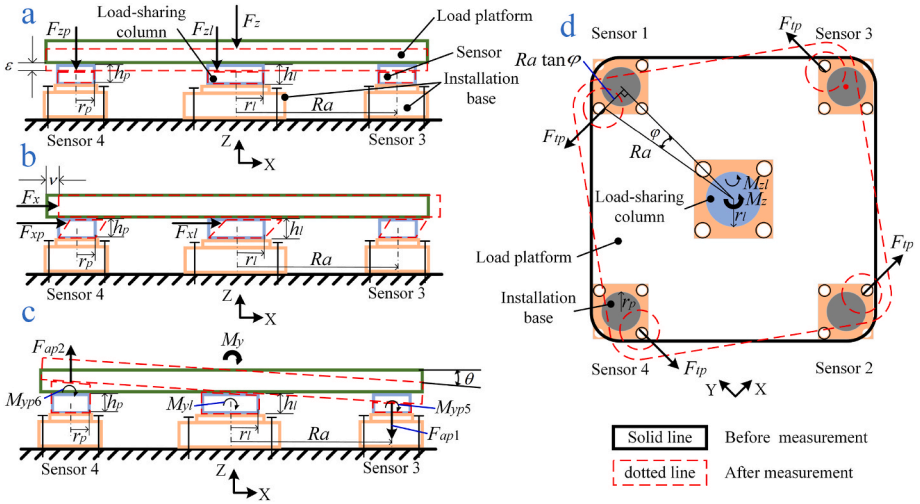

Fig. 3. Deformation of the platform under the action of forces/moments: (a) F_z; (b) F_x; (c) M_y; (d) M_z.

$$\begin{cases} Fzl\varepsilon l = \dfrac{Fzl^2 hl}{ElAl} \\ Fzp\varepsilon p = \dfrac{Fzp^2 hp}{EpAp} \end{cases} \tag{5}$$

Where E_l and E_p are the elastic modulus of the load-sharing column and the piezoelectric sensor, A_l and A_p are their cross-sectional areas, h_l and h_p are their heights, and ϵ_l and ϵ_p are their axial moving distances. Under the assumptions, ϵ_l and ϵ_p satisfy: $\epsilon_l = \epsilon_p = \epsilon$ (comparable in subsequent derivations).

Thus, μ_{Fz} can be obtained from Equations (2), (4) and (5):

$$\mu Fz = \frac{Fz - m}{Fz} = \frac{4Fzp}{4Fzp + Fzl} = \frac{4EpAphl}{4EpAphl + ElAlhp} = \frac{4Eprp^2 hl}{4Eprp^2 hl + Elrl^2 hp} \tag{6}$$

where r_l and r_p are the cross-sectional radius of the load-sharing column and the piezoelectric sensor, respectively.

3.2. Measurement coefficient of F_x

The derivation process of μ_{Fx} is similar to that of μ_{Fz}, and Equation (7) can be obtained from Fig. 3(b):

$$\begin{cases} Fx = 4Fxp + Fxl \\ Fxl\nu l = \dfrac{\mu lFxl^2 hl}{GlAl} \\ Fxp\nu p = \dfrac{\mu pFxp^2 hp}{GpAp} \\ \nu l = \nu p = \nu \end{cases} \tag{7}$$

where F_{xl} and F_{xp} are the shear forces acting on the column and the sensor, ν_l and ν_p are their horizontal moving distances, and G_l and G_p are their material shear modulus. μ_l and μ_p are non-uniformity coefficients for the distribution of cross-sections under shear stress, and as their cross-sections are all circular, $\mu_l = \mu_p = 10/9$.

The derivation based on Equations (2) and (7) gives μ_{Fx}:

$$\mu Fx = \frac{Fx - m}{Fx} = \frac{4Fxp}{4Fxp + Fxl} = \frac{4GpAp\mu lhl}{4GpAp\mu lhl + GlAl\mu php} = \frac{4Gprp^2 hl}{4Gprp^2 hl + Glrl^2 hp} \tag{8}$$

3.3. Measurement coefficient of M_y

It can be easily seen from Fig. 3(c) that when the load platform is subjected to M_y, the load-sharing column, sensor 1 and sensor 2 are only subjected to bending forces, while sensor 3 and sensor 4 are subjected to axial tensile forces (F_{api}, $i = 1, 2$) and bending forces. M_{yl} represents the moment acting on the load-sharing column, and M_{ypi} ($i = 3, 4, 5, 6$) is used to represent the moments acting on the four sensors. M_{yp1} and M_{yp2} represent the axial tensile forces acting on sensors 3 and 4 multiplied by the force arm, and it is these two that can be measured by the sensors. It thus follows that:

$$\begin{cases} My = Myl + \sum_{i=1}^{6} Mypi = Myl + Ra(Fap1 + Fap2) + \sum_{i=3}^{6} Mypi \\ Myl\theta l = \dfrac{Myl^2 hl}{ElIyl} \\ FapiRa\tan\theta p = \dfrac{Fapi^2 hp}{EpAp}, i = 1, 2 \\ Mypi\theta p = \dfrac{Mypi^2 hp}{EpIyp}, i = 3, 4, 5, 6 \\ \theta l = \theta p = \theta \end{cases} \tag{9}$$

where I_{yl} and I_{yp} are their inertia moments. The derivation of Equations (2) and (9) yields μ_{My}:

$$\mu My = \frac{My - m}{My} = \frac{\sum_{i=1}^{2} Mypi}{Myl + \sum_{i=1}^{6} Mypi} = \frac{Ra(Fap1 + Fap2)}{Ra(Fap1 + Fap2) + Myl + \sum_{i=3}^{6} Mypi} = \frac{2Ra^2 \tan\theta EpAphl}{2Ra^2 \tan\theta EpAphl + \theta ElIylhp + 4\theta EpIyphl} = \frac{2Ra^2 Ep\pi rp^2 hl}{2Ephl(\pi rp^2 Ra^2 + 2Iyp) + ElIylhp} \tag{10}$$

3.4. Measurement coefficient of M_z

As shown in Fig. 3(d), when the load platform is subjected to M_z, the load-sharing column is subjected to a torsional force M_{zl}, while the sensor is subjected to a shear force F_{tp} along the tangent line. It follows that:

$$\begin{cases} Mz = Mzl + 4Mzp = Mzl + 4RaFtp \\ Mzl\varphi l = \dfrac{Mzl^2 hl}{GlIzl} \\ FtpRa\tan\varphi p = \dfrac{\mu pFtp^2 hp}{GpAp} \\ \varphi l = \varphi p = \varphi \\ \mu p = \dfrac{10}{9} \end{cases} \tag{11}$$

Deriving Equations (2) and (11) gives μ_{Mz}:

$$\mu Mz = \frac{Mz - m}{Mz} = \frac{4RaFtp}{4RaFtp + Mzl} = \frac{4Ra^2 \tan\varphi GpAphl}{4Ra^2 \tan\varphi GpAphl + GlIzl\varphi\mu php} = \frac{36Ra^2 Gp\pi rp^2 hl}{36Ra^2 Gp\pi rp^2 hl + 10GlIzlhp} \tag{12}$$

The six-dimensional generalized forces acting on the load platform can thus be derived theoretically by Equations ((1), (2), (6), (8), (10) and (12).

4. Optimization and finite element simulation

The above calculations are based on four assumptions, but they are hard to fully satisfy in practice, resulting in the following conditions not necessarily holding in derivation:

$$\varepsilon l = \varepsilon p = \varepsilon, \nu l = \nu p = \nu, \theta l = \theta p = \theta, \varphi l = \varphi p = \varphi \tag{13}$$

Therefore, it is essential to investigate the influences of the platform parameters on the accuracy of the previous theoretical models. It is also necessary to research their effects on the measurement coefficients and fundamental frequency to provide a reference for the platform's design (for brevity, coefficients and frequency are used in the following discussion). The following is known: the smaller the coefficients are, the greater the platform's loading capacity is; the higher the platform's frequency is, the lower the resonance with the vibration source is, and the more accurate the measurements are.

The method for studying the effects of structural parameters on platform performance is illustrated in Fig. 4 [1]. The platform structural parameters appearing in Equations ((6), (8), (10) and (12) can be used as variables for the study, while the errors $\triangle\mu$ between the theoretical measurement coefficients and simulations, the coefficients μ and the frequency Fq are used as objective functions (evaluation indicators). In order to satisfy conditions (1) and (2) in the assumptions as far as possible, stainless steel was chosen as the material for the load platform and installation bases and aluminum alloy for the load-sharing column. Table 1 shows the material properties of the platform components, where the parameters of the sensor are experimentally measured. Once the materials of the structures have been selected, their material

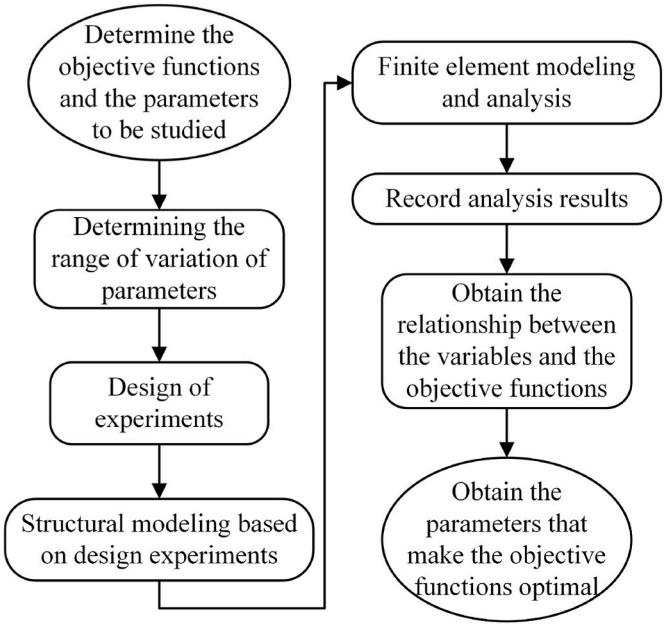

Fig. 4. Flowchart of the research method [1].

Table 1
Material properties of platform components.

Components	E (MPa)	ν	P (kg/m^3)
Load platform & Installation base	2.06×10^5	0.3	7.85×10^3
Load-sharing column	7×10^4	0.33	2.8×10^3
Sensors	7.65×10^4	0.32	7.5×10^3

properties are no longer considered variables. The range of variables selected and the evaluation indicators are shown in Table 2. Where six design variables are the radius of the load-sharing column r_l, the radius of the sensor r_p, the height of the load-sharing column h_l, the height of the sensor h_p, the height of the load platform H and the radius of the sensor distribution Ra.

Experiment design can be done in a variety of ways [25–28]. The BBD was chosen because it avoids the appearance of extreme points, making it appropriate for optimization of structural size [29]. 54 sets of tests were created by Expert-Design using the BBD. Models for each set were built, finite element simulations were carried out, and the values of the objective function were saved (all finished using script codes). According to a statistical analysis of the findings, all objective functions match the standards (according to article [1]), and Figs. 5–13 depict the connection between the objective functions and the structural parameter variables.

It can be obtained from the previous figures that as r_p becomes larger, all coefficients and frequency increasingly become larger. $\triangle\mu_{Fz}$ and $\triangle\mu_{My}$ decrease at the beginning and then increase, while $\triangle\mu_{Fx}$ and $\triangle\mu_{Mz}$ continue to decrease.

As r_l becomes larger (the moment of inertia also changes), all the measurement coefficients continue to decrease, and the platform fundamental frequency increases. $\triangle\mu_{Fz}$ decreases at the beginning and then increases, while there is no effect on $\triangle\mu_{Fz}$. $\triangle\mu_{My}$ decreases and then increases, and $\triangle\mu_{Mz}$ continues to increase.

Accompanying h_l becomes larger, all the coefficients become larger increasingly, and the frequency decreases slightly. $\triangle\mu_{Fz}$, $\triangle\mu_{My}$ decrease and then increase, while $\triangle\mu_{Fx}$ increases at the beginning and then decreases. $\triangle\mu_{Mz}$ continues to decrease.

With h_p becoming larger, all coefficients decrease increasingly, while the frequency decrease significantly. $\triangle\mu_{Fz}$ and $\triangle\mu_{Fx}$ decrease at the beginning and increase later. $\triangle\mu_{My}$ continues to decrease when h_l is large, while $\triangle\mu_{My}$ decreases when h_l is small. $\triangle\mu_{Mz}$ continues to become larger.

When H becomes larger, there is basically no effect on all coefficients, while the frequency decreases. Except for a small increase in $\triangle\mu_{My}$, there is almost no effect on the remaining errors.

Following the increase in Ra, μ_{My} and μ_{Mz} continue to increase, where μ_{Mz} increases slightly, and there is essentially no effect on the rest of the coefficients. The frequency continues to rise at the beginning and later remains unchanged. $\triangle\mu_{Fx}$ increases and then decreases slightly, while $\triangle\mu_{Mz}$ continues to decrease. There is no effect on the rest of the errors.

The trend of the coefficients is consistent with the theoretical models as the parameters vary. However, because of the possibility of storing energy during the force action (for example, due to the deformation of the load platform and installation bases), there are some errors between the theories and the simulations. Of course, the control variable method can also be used to verify the correctness of the proposed models, but it does not provide reliable structural optimization and is therefore not used.

According to the relationship between the above parameter variables and the objective functions, the regression equations between these two can be fitted. Combining the regression equations and the optimization problem, the structural parameters can be obtained, which make the coefficients and their errors as small as possible and the fundamental frequency as large as possible. A set of optimal structural parameters and the objective function values are shown as the Optimal value in Table 2, which is very close to the Theoretical value. However, as some of the simulation parameters of the sensor are obtained roughly by experiment, errors are unavoidable.

The optimal structural parameters were used to re-establish the model, the model was meshed, and the finite element analysis was carried out as shown in Fig. 14(a) and (b). The simulation results are shown in Table 2, which show that the load-sharing column can have an obvious force-sharing effect (although the moment sharing effect is not obvious). The maximum load capacity of 30 kN can also be obtained through the simulation, which is more than enough to meet the measurement requirements.

Based on these optimal structural parameters, a model of the platform without the column was constructed, and the platform's fundamental frequency is 1386 Hz, as shown in Fig. 14(c), which means that the fundamental frequency of the measurement platform with the load-sharing column has been significantly increased. The higher the platform's fundamental frequency is, the smaller the vibration coupling with the measured source is, and the higher the measuring accuracy is. What's more, it can be calculated from Equation (6) that the load capacity of the platform with a column is 59.7% higher than that of the platform without a column. Therefore, the platform without the column is not chosen.

Table 2
Range of variables, evaluation indicators, optimal parameters, and theoretical and simulation results.

Operations	Variables						Objective functions								
	r_l	r_p	h_l	h_p	H	Ra	μ_{Fx}	μ_{Fz}	μ_{My}	μ_{Mz}	Fq	$\triangle\mu_{Fx}$	$\triangle\mu_{Fz}$	$\triangle\mu_{My}$	$\triangle\mu_{Mz}$
Range (mm) or Target	15–35	7.5–20	10–40	10–40	20–50	160–254	min	min	min	min	max	min	min	min	min
Optimal value (mm)	35	14.9	24.4	10	39.3	224.8	0.627	0.619	0.992	0.915	1671	0.035	0.052	0.008	0.021
Theoretical value (mm)	35	14.9	24.4	10	39.3	224.8	0.638	0.638	0.991	0.909	–	–	–	–	–
Simulation value (mm)	35	14.9	24.4	10	39.3	224.8	0.616	0.603	0.986	0.921	1793	–	–	–	–

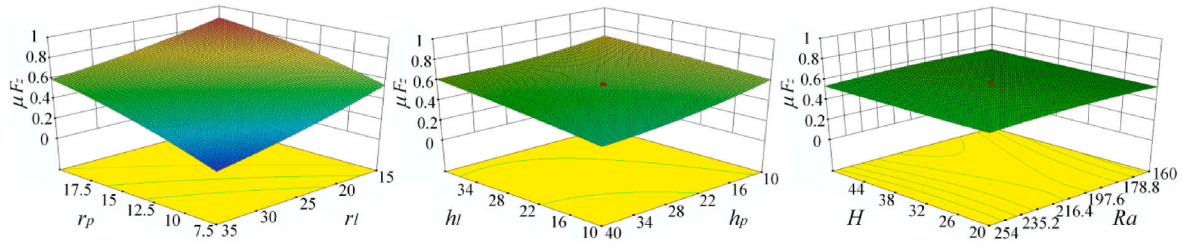

Fig. 5. Response surface for μ_{Fz} versus variables of the structural parameters.

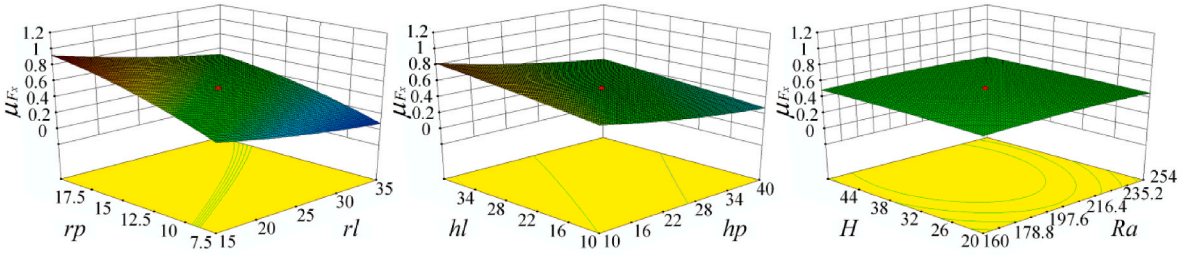

Fig. 6. Response surface for μ_{Fx} versus variables of the structural parameters.

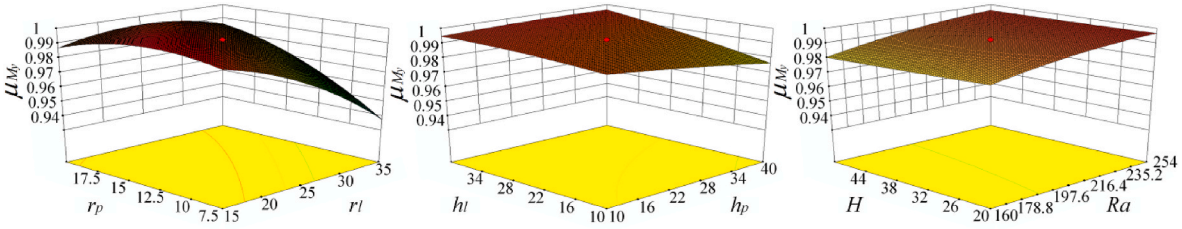

Fig. 7. Response surface for μ_{My} versus variables of the structural parameters.

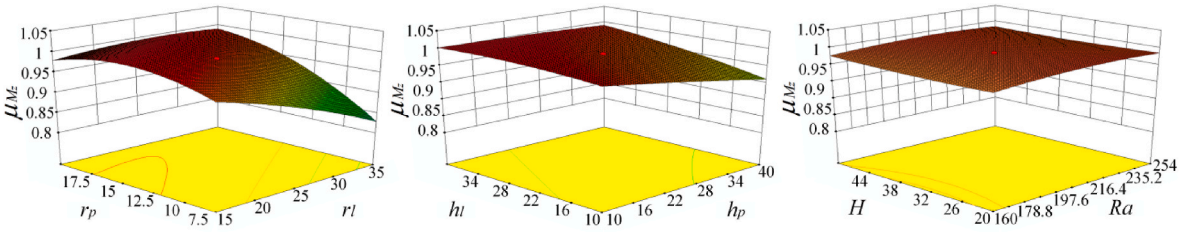

Fig. 8. Response surface for μ_{Mz} versus variables of the structural parameters.

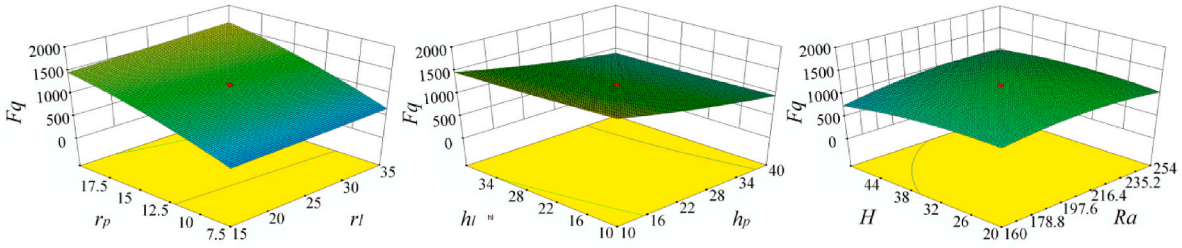

Fig. 9. Response surface for *Fq* versus variables of the structural parameters.

Besides, finite element analysis can also be used to examine the inter-dimensional coupling and static linearity of the measurement based on the platform with the column mentioned above. Forces (10 N–6000 N) and moments (10 Nm–600 Nm) were applied to the measurement platform, acting one force or moment in one direction at a time, and the results are shown in Fig. 15. From the figure, it can be deduced that the platform has weak inter-dimensional coupling and good self-decoupling capability. Moreover, the platform has good static linearity.

The previous analysis was based on the best parameters; now, a random set of parameters is chosen for the simulation shown in Fig. 15. The first subplot of Fig. 15 depicts the outputs of the non-optimal platform under a force acting in the X-direction. According to the results, its

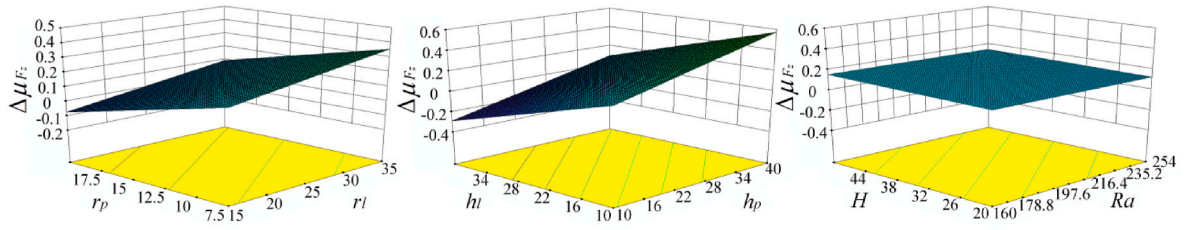

Fig. 10. Response surface for $\triangle\mu_{Fz}$ versus variables of the structural parameters.

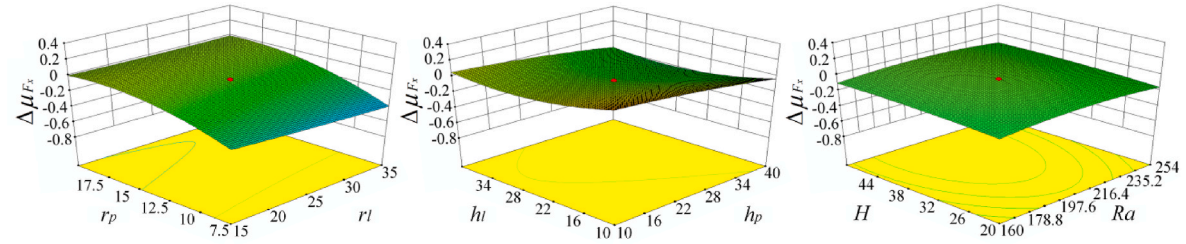

Fig. 11. Response surface for $\triangle\mu_{Fx}$ versus variables of the structural parameters.

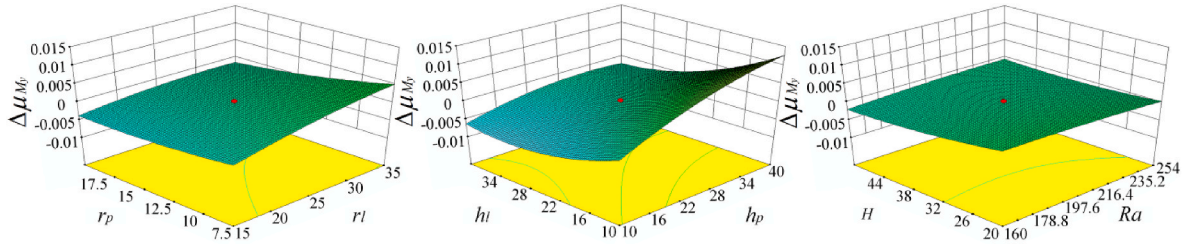

Fig. 12. Response surface for $\triangle\mu_{My}$ versus variables of the structural parameters.

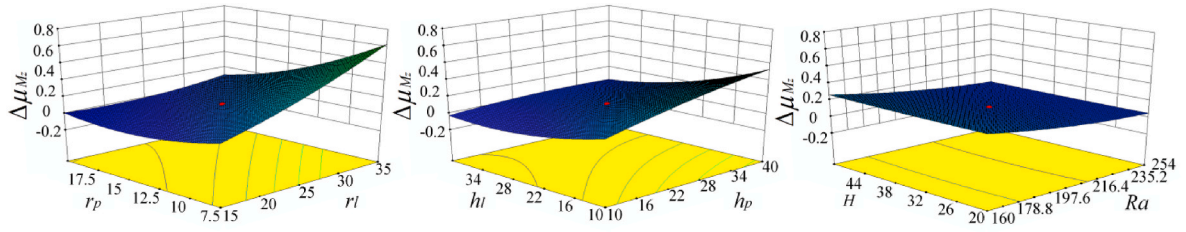

Fig. 13. Response surface for $\triangle\mu_{Mz}$ versus variables of the structural parameters.

load-sharing and decoupling capabilities are inferior to those of the platform based on the optimum parameters. However, the platform's basic structure ensures that its linearity is not significantly affected.

5. Experiment

A load-sharing-based measuring platform prototype was fabricated based on the theories and simulations mentioned above. The measurement coefficients of the platform were tested (as calibration), and the dynamic properties of the platform were also assessed. It should be mentioned that the theoretical mathematical models are proposed to provide a basis for the design and manufacture of the platform, but it is necessary to re-calibrate the platform in order to improve the measurement accuracy before measurement.

5.1. Verification of measurement coefficients

The measurement coefficient calibration system is depicted in Fig. 16, consisting of a load-sharing-based measurement platform, a calibration system (pulley system), a charge amplifier (5080A, Kistler), a digital data acquisition (VRAI820-24bit, M + P), and a PC. The charge amplifier turned on the charge-hold function.

A single-dimensional static force/moment was applied to the measurement system separately through the calibration system and was gradually increased from 0 N to 1000 N (0 Nm to 200 Nm), and the calibration was carried out three times. The input and average output forces/moments are shown in Fig. 17. According to Table 3, the proposed platform has good weak coupling, and the linearity error rate (data on the diagonal) of the system is less than 1%, which satisfy the measurement requirements and outperform the dynamic measurement platform proposed in the article [10], and the repeatability error is less than 0.2% FS. Besides, the fitted values of the four measurement coefficients are 0.608, 0.626, 0.971, and 0.924, respectively. The experimental results are in good accordance with the theoretical models and simulation results, and acceptable errors in the experimental results may originate from thermal effects, machining and installation errors, etc.

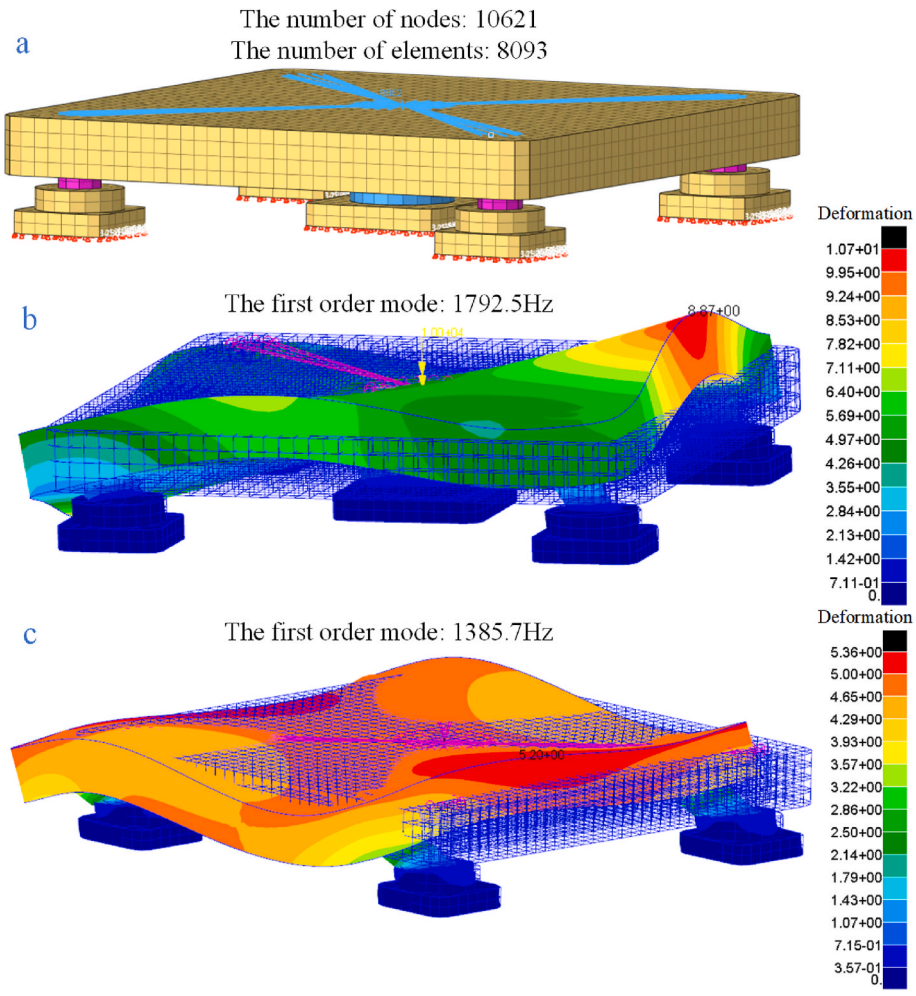

Fig. 14. Simulation of models based on optimal structural parameters: (a) meshed model with column; (b) the 1st order mode of the platform with column; (c) the 1st order mode of the platform without column.

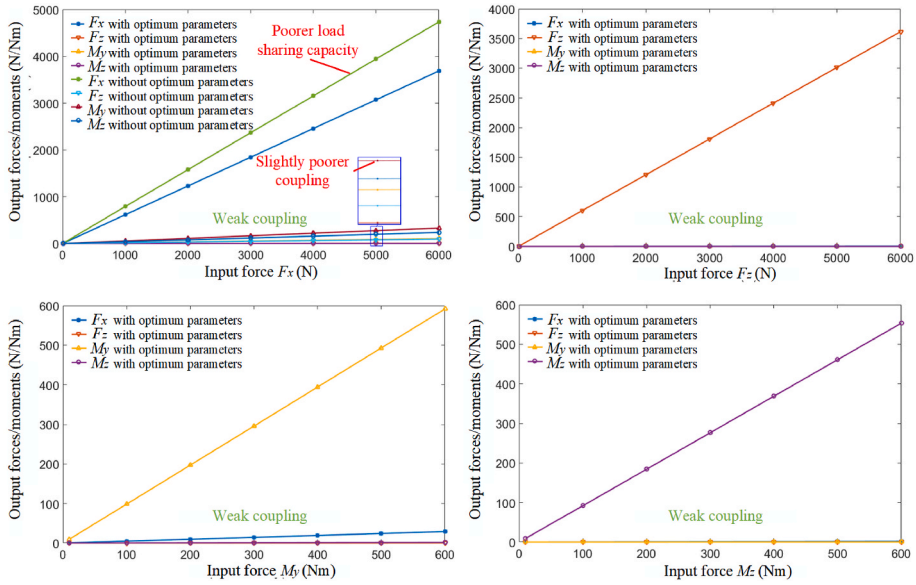

Fig. 15. Static inputs versus outputs of the load-sharing-based platform using FEA.

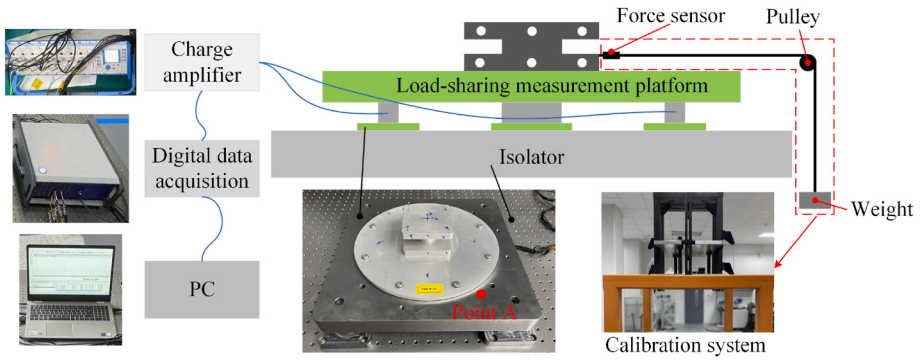

Fig. 16. Calibration system for measurement coefficients.

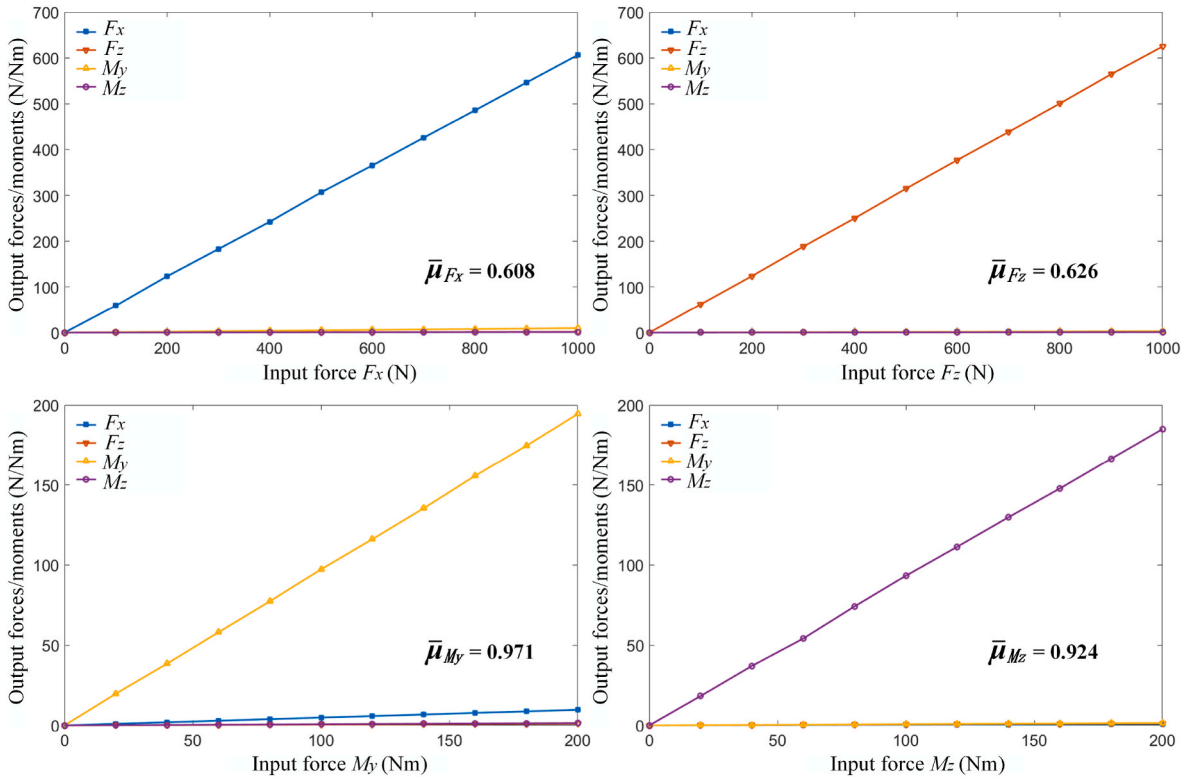

Fig. 17. Calibration curves for measurement coefficients.

Table 3
Coupling interference and static linearity of the measurement platform.

Force/moment (N/Nm)	Coupling interference and static linearity (%)			
	F_x	F_z	M_y	M_z
F_x	0.41	0.36	4.98	0.48
F_z	0.28	0.37	0.53	0.67
M_y	1.59	0.46	0.42	0.82
M_z	0.19	0.15	0.75	0.56

5.2. Test for dynamic performance

The dynamic characteristics will be tested next. The high fundamental frequency of the platform is the basis for its excellent dynamic characteristics, avoiding the possibility of the measured signal being amplified by the platform. Point A on the platform was selected casually, as depicted in Fig. 16, and three hammer blows of different force magnitudes were performed using a force hammer (5800B5, PCB). The transfer functions shown in Fig. 18 were obtained with a sampling frequency of 6400 Hz for 16 s. It can be obtained that the 1st order frequency of the platform is 1696 Hz, which is close to the simulated frequency of 1792 Hz. This fundamental frequency is high enough for the dynamic force measurements of the equipment on the spacecraft. It can also be observed that the dynamic linearity of the system is excellent, within 0.3% FS.

After that, the dynamic measurement accuracy of the load-sharing-based measurement platform under sinusoidal excitation was verified by using the shaker (K2004E01) to simulate the in-orbit vibration sources disturbances. The measurement system is shown in Fig. 19.

A single frequency excitation was input each time with the use of the shaker and measured with the use of the platform. To simulate the disturbance forces from the CMG and cryocooler in orbit, sinusoidal excitations of 46.7 Hz, 116.7 Hz, 233 Hz (simulation for the CMG), 80 Hz, 160 Hz and 240 Hz (simulation for the cryocooler) were input. In addition, 5 Hz and 1000 Hz (avoiding the interference of the isolator as shown in the red box in Fig. 18) excitations were input to evaluate the low and high frequency properties of the platform. The inputs and

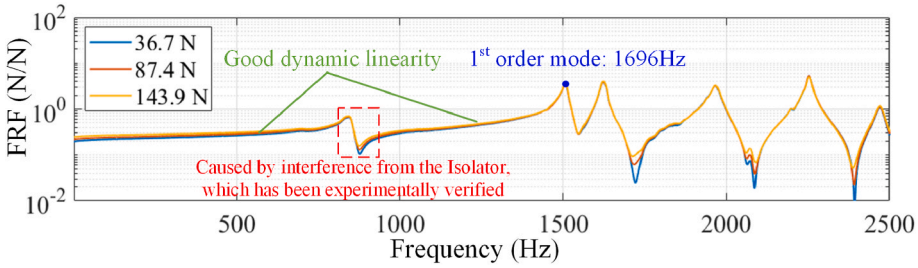

Fig. 18. Transfer function curves for three different forces.

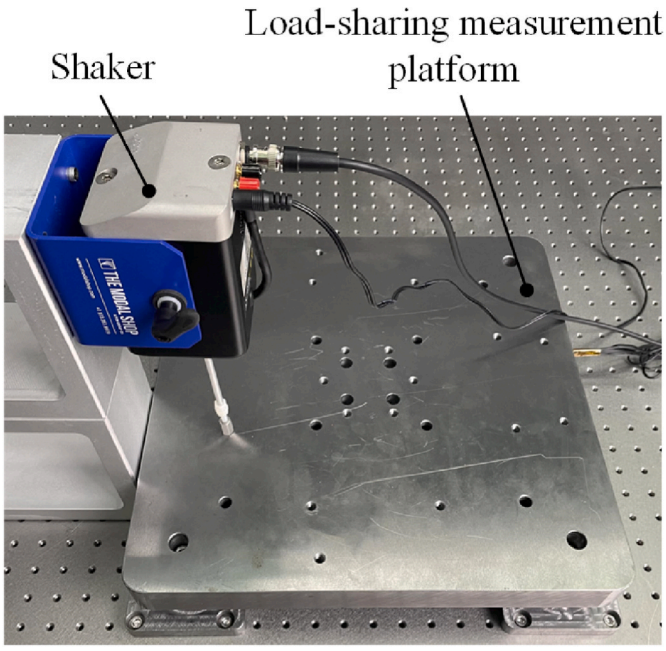

Fig. 19. The measurement platform with a shaker.

outputs of the simulated disturbance forces in the X direction are shown in Fig. 20, and the data of forces/moments in the six directions is summarized in Table 4. As can be observed from the table, the measurement accuracy is high for the majority of frequencies, except for the measurement at 5 Hz, where there is a large error caused by the poor dynamic characteristics of the piezoelectric ceramic at low frequencies. The average dynamic error rate of the platform is within 6%, and the relative errors' RMS values are less than 3.7×10^{-4} N and 4.4×10^{-5} Nm, which meets the measuring needs.

Finally, to further validate the accuracy of the platform over the entire frequency band, the impulse forces were input using a force hammer and measured with the platform. The results in two directions are shown in Fig. 21. The average dynamic accuracy of the six-dimensional forces over the entire frequency band can be guaranteed to be within 5.5%.

6. Conclusion

This paper proposes a piezoelectric load-sharing-based measurement platform for measuring dynamic six-dimensional disturbance forces/moments from large equipment. Firstly, the set-up of the load-sharing column not only increases the fundamental frequency of the platform but also significantly increases its load capacity. Two types of piezoelectric-ceramic-based sensors are mounted on the four corners of the platform in the form of spokes. The installation of two different kinds of sensors lowers the manufacturing cost of the platform on the one hand and ensures complete measurement of the six-dimensional forces/moments on the other. Secondly, the measurement principle and essential measurement coefficients are derived for the designed platform. Finite element analysis is then used to investigate the influence of the platform's structural parameters on the platform's performance and the accuracy of the mathematical measurement models, which gives a basis for the design and manufacture of the platform and shortens the development cycle of the platform. Finally, experiments are carried out with the fabricated prototype. The experimental results show that the four measured measurement coefficients are 0.608, 0.626, 0.971, and 0.924, and the platform's fundamental frequency is 1696 Hz, which are in good agreement with the theoretical derivation. It can be inferred that the load capacity of the load-sharing-based measuring platform is increased by 59.7% and the fundamental frequency by 22.4% compared to the platform without the load-sharing column. In addition, the average dynamic measurement error rate of the designed platform is measured to be within 6%, while the measurement platform has good self-decoupling and both static and dynamic linearity. The study shows

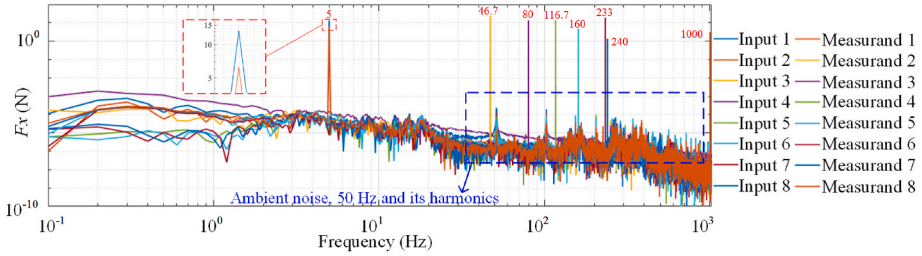

Fig. 20. Input force of F_x generated by the shaker compared to the output force measured by the load-sharing-based platform.

Table 4
Data of the input forces in six directions from the shaker and the measured forces from the load-sharing-based platform.

Frequency (Hz)		5	46.7	80	116.7	160	233	240	1000
F_x (N)	Input	13.4	24.59	13.60	14.21	4.85	18.78	1.47	2.74
	Measured	6.29	24.54	13.57	13.87	4.49	18.91	1.35	3.12
F_y (N)	Input	11.6	22.12	11.31	10.89	3.72	10.07	1.53	3.44
	Measured	4.23	22.05	11.36	10.54	3.67	9.94	1.51	3.32
F_z (N)	Input	23.51	12.45	34.09	19.83	15.74	3.88	5.77	4.10
	Measured	15.61	11.72	33.65	20.16	15.50	3.89	6.15	3.98
M_x (Nm)	Input	5.12	8.69	9.67	7.81	5.12	4.74	1.36	0.18
	Measured	7.23	8.53	9.43	8.08	5.36	4.89	1.34	0.17
M_y (Nm)	Input	4.62	10.74	12.41	7.84	6.83	3.44	1.21	0.16
	Measured	11.50	10.71	12.45	7.83	6.76	3.39	1.24	0.17
M_z (Nm)	Input	1.36	12.37	10.23	9.69	9.37	8.31	7.93	0.15
	Measured	3.22	12.23	10.11	9.63	9.29	8.20	8.03	0.16

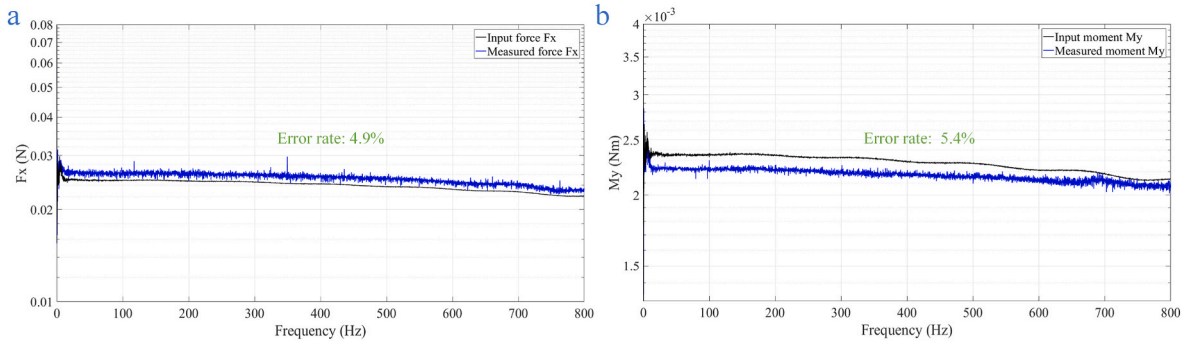

Fig. 21. Input impulse forces versus output forces: (a) F_x; (b) M_y.

that the proposed measurement platform performs admirably in terms of cost, fundamental frequency, loading capacity, and measurement accuracy. It can meet the requirements for dynamic measurement of vibration sources on board spacecraft, and the article provides a reference for the design of a similar measurement platform.

Funding

This work was supported by the National Natural Science Foundation of China (No. 11972343) and the National Natural Science Foundation of China (No. 62235018).

Declaration of competing interest

The authors declare that they have no known competing financial interests or personal relationships that could have appeared to influence the work reported in this paper.

Acknowledgment

We thank Kaiying for her assistance throughout the research process, including care, tolerance, etc.

References

[1] Zhou CB, Xia MY, Xu ZB. Design and optimization of a quadrupedal dynamic disturbance force measurement platform using strain gauges. Mech Syst Signal Process 2022:110032. https://doi.org/10.1016/j.ymssp. 2022.110032.
[2] Zhou CB, Xia MY, Xu ZB. A six dimensional dynamic force/moment measurement platform based on matrix sensors designed for large equipment. Sensor Actuator Phys 2022:114085. https://doi.org/10.1016/j.sna.2022.114085.
[3] Sun Y, Deng DS, Yuan HB. Precision of the Chinese space station telescope (CSST) stellar radial velocities. Res Astron Astrophys 2021;21(4):92. https://doi.org/10.1088/1674-4527/21/4/92.
[4] Cao Y, Gong Y, Zheng ZY, et al. Calibrating photometric redshift measurements with the multi-channel imager (MCI) of the China space station telescope (CSST). Res Astron Astrophys 2022;22(2):025019. https://doi.org/10.1088/1674-4527/ac424e.
[5] Zhan H. An overview of the Chinese space station optical survey. 42nd COSPAR Scientific Assembly 2018;42:E1–16. https://ui.adsabs.harvard.edu/abs/2018cosp...42E3821Z.
[6] Gong Y, et al. Cosmology from the Chinese space station optical survey (CSS-OS). Astrophys J 2019;883(2):203. https://doi.org/10.3847/1538-4357/ab391e.
[7] Li CY, et al. Searching for multiple populations in star clusters using the China Space Station Telescope. Res Astron Astrophys 2022;22(9):095004. https://doi.org/10.1088/1674-4527/ac7bf1.
[8] Yang JF, et al. Design of a vibration isolation system for the space telescope. J Guid Control Dynam 2015;38(12):2441–8. https://doi.org/10.2514/1.G001221.
[9] Toyoshima M, et al. In-orbit measurements of spacecraft microvibrations for satellite laser communication links. Opt Eng 2010;49(8). https://doi.org/10.1117/1.3482165. 083604-083604.
[10] Xia MY, Xu ZB, Han K, Huo Q, Li A. Dynamic disturbance force measurement platform for large moving device in spacecraft. J Sound Vib 2019;447:61–77. https://doi.org/10.1016/j.jsv.2019.01.053.
[11] Li L, Tan L, Kong L, Wang D, Yang H. The influence of flywheel micro vibration on space camera and vibration suppression. Mech Syst Signal Process 2018;100:360–70. https://doi.org/10.1016/j.ymssp.2017.07.029.
[12] Liang QK, Zhang D, Song QJ, et al. Design and fabrication of a six-dimensional wrist force/torque sensor based on E-type membranes compared to cross beams. Measurement 2010;43(10):1702–19. https://doi.org/10.1016/j.measurement.2010.09. 010.
[13] Wu B, Luo J, Shen F, et al. Optimum design method of multi-axis force sensor integrated in humanoid robot foot system. Measurement 2011;44(9):1651–60. https://doi.org/10.1016/j. measurement.2011.06.013.
[14] Ma JQ, Song AG. Fast estimation of strains for cross-beams six-axis force/torque sensors by mechanical modeling. Sensors 2013;13(5):6669–86. https://doi.org/10.3390/s130506669.
[15] Sun YJ, et al. Design and optimization of a novel six-axis force/torque sensor for space robot. Measurement 2015;65:135–48. https://doi.org/10.1016/j.measurement.2015.01.005.
[16] Han K, et al. Design and optimization of a high sensitivity joint torque sensor for robot fingers. Measurement 2020;152:107328. https://doi.org/10.1016/j.measurement.2019.107328.
[17] Huang Z, Chen SH, Wang HY. Development of three-dimensional dynamic grinding force measurement platform. Proc IME C J Mech Eng Sci 2018;232(2):331–40. https://doi.org/10.1177/0954406216680380.
[18] Jia ZY, Lin S, Liu W. Measurement method of six-axis load sharing based on the Stewart platform. Measurement 2010;43(3):329–35. https://doi.org/10.1016/j.measurement.2009.11.005.
[19] Li YJ, et al. Dynamic characteristics of piezoelectric six-dimensional heavy force/moment sensor for large-load robotic manipulator. Measurement 2012;45(5):1114–25. https://doi.org/10.1016/j.measurement.2012.01.028.

[20] Li YJ, Zhang J, Jia ZY, et al. Research on a novel parallel spoke piezoelectric 6-DOF heavy force/torque sensor. Mech Syst Signal Process 2013;36(1):152–67. https://doi.org/10.1016/j.ymssp.2012.03.016.
[21] Li YJ, et al. Research on the parallel load sharing principle of a novel self-decoupled piezoelectric six-dimensional force sensor. ISA Trans 2017;70:447–57. https://doi.org/10.1016/j.isatra.2017.07.008.
[22] Liu J, et al. Active design method for the static characteristics of a piezoelectric six-axis force/torque sensor. Sensors 2014;14(1):659–71. https://doi.org/10.3390/s140100659.
[23] Li YJ, et al. Research on static decoupling algorithm for piezoelectric six axis force/torque sensor based on LSSVR fusion algorithm. Mech Syst Signal Process 2018;110:509–20. https://doi.org/10.1016/j.ymssp.2018.03.015.
[24] Li YJ, et al. A novel parallel piezoelectric six-axis heavy force/torque sensor. Measurement 2009;42(5):730–6. https://doi.org/10.1016/j.measurement.2008.12.005.
[25] Li YJ, Zhang J, Jia ZY, et al. A novel piezoelectric 6-component heavy force/moment sensor for huge heavy-load manipulator's gripper. Mech Syst Signal Process 2009;23(5):1644–51. https://doi.org/10.1016/j.ymssp.2009. 02.004.
[26] Khuri, et al. Response surface methodology. Wiley Interdisciplinary Reviews: Comput Stat 2010;2(2):128–49. https://doi.org/10.1002/wics.73.
[27] Box GEP, Wilson KB. On the experimental attainment of optimum conditions. Breakthroughs in statistics. New York, NY: Springer; 1992. p. 270–310. https://doi.org/10.1007/978-1- 4612 -4380-9_23.
[28] Reddy TA. Applied data analysis and modeling for energy engineers and scientists. Springer Science & Business Media; 2011.
[29] Ferreira SLC, Bruns RE, Ferreira HS, et al. Box-Behnken design: an alternative for the optimization of analytical methods. Anal Chim Acta 2007;597(2):179–86. https://doi.org/10.1016/j.aca.2007.07.011.